Full length article

An investigation of diffusion-mediated cyclic coarsening and reversal coarsening in an advanced Ni-based superalloy

Yiqiang Chen [a], R. Prasath babu [a], Thomas J.A. Slater [a], Mingwen Bai [a], Robert Mitchell [b], Octav Ciuca [a], Michael Preuss [a], Sarah J. Haigh [a], *

[a] School of Materials, University of Manchester, MSS Building, Sackville Street, Manchester, M13 9PL, UK
[b] Rolls-Royce plc, PO Box 31, Derby, DE24 8BJ, UK

ARTICLE INFO

ABSTRACT

The anomalous cyclic coarsening behaviour of γ' precipitates after ageing at 1073 K has been investigated for the low misfit commercial powder metallurgy (PM) Ni-based superalloy RR1000. Using scanning transmission electron microscope (STEM) imaging combined with absorption-corrected energy-dispersive X-ray (EDX) spectroscopy, the elemental segregation as a function of coarsening behaviour has been experimentally observed for secondary γ' precipitates. Elemental EDX spectrum imaging has revealed nanoscale enrichment of Co and Cr and a depletion of Al and Ti within the γ matrix close to the γ-γ' interface. Our experimental results, coupled with complementary modelling and synchrotron X-ray diffraction analysis, demonstrate the importance of elastic strain energy resulting from local compositional variations for influencing precipitate morphology. In particular, elemental inhomogeneities, as a result of complex diffusive interactions within both matrix and precipitates, play a crucial role in determining the rate of coarsening. Our findings provide important new evidence for understanding the microstructural evolution observed for advanced superalloys when they are exposed to different heat treatment regimes.

1. Introduction

Nickel-based superalloys for turbine disc applications typically employ complex alloy chemistry in order to produce a stable, high volume fraction of gamma-prime (γ') precipitates to optimise mechanical properties at elevated temperature [1,2]. Precipitate coarsening causes a gradual loss of coherency between the γ' precipitates and γ matrix which can be detrimental to the superalloy's mechanical performance [3,4]. This coarsening process is relatively well understood for a binary system. However, the complex chemistry present within commercial Ni-based superalloys makes it extremely challenging to accurately predict the microstructural evolution for precipitate coarsening of these materials. A more accurate understanding of coarsening mechanisms is required in order to control the rate of coarsening for both current and next-generation superalloys.

The thermodynamic driving force for microstructural coarsening is generally dominated by the reduction in free energy achievable by minimising the system's interfacial energy. In contrast, the rate of coarsening is determined by the speed of interface migration or by elemental diffusion kinetics [5]. For ordered γ' precipitates within Ni-based superalloys, the growth rate of precipitates during coarsening is conventionally assumed to be controlled by diffusion kinetics in the γ matrix [6]. Within this matrix diffusion-controlled coarsening (MDC) regime, the average precipitate radius, $<r>$, is predicted to increase according to a classical Lifshitz-Slyozov-Wagner (LSW) theory such that $<r>^3 \approx k(f)t$ [6] where $k(f)$ is the rate of coarsening, f the volume fraction of precipitates and t time [6]. Classical LSW theory requires that the volume-fraction of precipitates is small but modifications exist for systems where the volume-fraction of precipitates is high, and therefore particles cannot be assumed to grow independently [7]. Classical LSW theory also assumes that the precipitate–matrix interface is atomically sharp but state-of-the-art high-resolution characterisation techniques are increasingly providing data showing that this is not true. For example, Singh et al. have used atom probe tomography (APT) to study the γ-γ' interface in the alloy Rene88 and found it has a diffusive width of ~2 nm [8–10].

Ardell et al. have used a quantum kinetic Monte Carlo method to predict that even in a simple Ni–Al binary system the γ-γ′ interface has a characteristic ragged morphology and a width of a few atomic layers at 700 K which increases at higher temperatures [11,12]. Most alloying elements diffuse orders of magnitude more slowly within the ordered intermetallic L1$_2$ structure of the γ′ precipitates, than in the FCC γ matrix [13–17]. As a consequence, matrix regions near the γ-γ′ interface may become a bottleneck for diffusion resulting in diffusive interfaces. The exceptionally low γ-γ′ interfacial energy (~10 mJ/m^2) will also favour a wide diffusive interface as predicted in Ref. [18]. Ardell et al. [11,12] proposed a trans-interface-diffusion-controlled coarsening (TIDC) model to account for experimentally observed coarsening behaviour in binary Ni–Al alloys and ternary Ni–Al–Cr alloys with high volume fractions of γ′ precipitates. Both interface migration-controlled coarsening (IMC) and TIDC predict $<r>^2 \propto t$, [19]. However, in real alloy systems, interactions between different diffusing species can alter the interdiffusion kinetics [17] and as a result, $<r>^\alpha \propto t$ where $2 < \alpha < 3$ and, $\alpha \sim 2.5$ in Ni–Al and Ni–Al–Cr alloy systems [12].

The simple coarsening models mentioned above also assume that the γ-γ′ coherency strain is negligible. However, the experimental observation of reversal coarsening, i.e., the splitting of large precipitates into smaller precipitates both in simple model alloys [3,20–22] and in commercial nickel based superalloys [20] indicates the contrary: that elastic strain energy is important in the coarsening process. Indeed, it has been argued that for superalloys with a high volume fraction of γ′, strong elastic constraints between neighbouring precipitates will lead to a decrease in precipitate size during ageing (for example, causing cubic γ′ precipitates to split into smaller cuboids [3,20,21]). Only by inclusion of microelasticity theory with the consideration of elastic interaction into the coarsening models can these morphological transitions be understood [3,20,21,23].

Precipitate splitting is most likely to occur for cuboidal γ′ precipitates in Ni-based superalloys where there is a relatively large lattice misfit. In these materials, high elastic strain energy can cause morphological instability such that the precipitates divide into smaller precipitates to lower the total energy of the system [22]. Here we report new experimental observations of abnormal cyclic coarsening and reversal coarsening (i.e. splitting) for nearly spherical γ′ precipitates in a near-zero misfit alloy RR1000. Secondary γ′ precipitates are found to coarsen periodically in a manner that differs from previous results [3,21], and which correlates to localised (nanoscale) elemental segregations resulting from limited elemental diffusivities. In particular, our results highlight the importance of diffusion kinetics when predicting precipitate coarsening and demonstrate the need to incorporate these into theoretical models for accurate prediction of microstructural evolution during γ′ coarsening in advanced Ni-based superalloys.

2. Experimental details

2.1. Materials and heat treatment

The commercial Ni-based superalloy RR1000, studied in the present work, has the nominal composition shown in Table. 1 and is used for disc applications in aero engines. This polycrystalline Ni-based superalloy is manufactured via the powder metallurgical route followed by subsequent forging, and typically exhibits a tri-modal γ′ particle size distribution (PSD) [24]. In this work, blanks of size $5 \times 5 \times 5$ mm^3 were first heat treated for 2 h at a supersolvus temperature (20 K above the γ′-solvus) in order to homogenise the microstructure and chemistry of the material. These blanks were cooled to room temperature using a controlled cooling rate of 100 K/min. The material was aged subsequently at 1073 K for different annealing time (as-cooled to 8 h with a step size of 0.5 h) and water quenched in order to study the microstructural evolution during coarsening. The heat treatment conditions were accurately controlled using a thermocouple fitted into the centre of an equivalent block of specimen to continuously monitor the temperature and cooling rate for the material.

2.2. Synchrotron X-ray diffraction

Accurate γ-γ′ lattice coherency strain measurements are notoriously difficult as the misfit strain between the two phases is generally too small to allow simple separation of the respective fundamental reflections. Hence, any accurate analysis requires the additional measurement of the γ′ superlattice reflections as they provide unambiguous information of the γ′ lattice spacing, which can be employed to deconvolute the strongly overlapping fundamental γ/γ′ reflection. However, these superlattice reflections are far too weak to be analysed via conventional laboratory scale X-ray diffraction (XRD) techniques, but instead require the use of either synchrotron XRD [20,25] or neutron diffraction [26,27]. In the present case, high energy, high resolution diffraction analysis was performed on beamline ID31 at the European Synchrotron Radiation Facility (ESRF, Grenoble, France) for bulk and extracted γ′ powder samples. Scans were carried out to compare constrained and unconstrained lattice spacings measured from bulk and extracted γ′ powder samples, respectively. Samples were heated to 1073 K in a capillary in order to minimize oxidation effects and held at this temperature during measurement. The constrained γ-γ′ coherency strain was determined as [20]:

$$\varepsilon_{constrained} = \left(a_{\gamma'}^{bulk} - a_{\gamma}^{bulk} \right) \Big/ \left(a_{\gamma}^{bulk} \right)$$

where $a_{\gamma'}^{bulk}$, a_{γ}^{bulk} are the lattice parameters of γ′ and γ, respectively. The γ-γ′ coherency strain was gained by first determining the position of the γ′ {100} superlattice reflection and using this information to deconvolute the {400} fundamental reflections for γ and γ′. The unconstrained lattice parameter for γ′ in the extracted precipitates was also derived using the same {400} reflection so as to calculate the unconstrained coherency strain [20]:

$$\varepsilon_{unconstrained} = \left(a_{\gamma'}^{powder} - a_{\gamma}^{bulk} \right) \Big/ \left(a_{\gamma}^{bulk} \right)$$

where $a_{\gamma'}^{powder}$, is the lattice parameter of γ′ within the extracted γ′ powder sample. Using peak deconvolution, the typical error in these measurements allows the misfit to be calculated with an accuracy of ±0.005% [20]. We note that these measurements include information averaged over millions of grains containing

Table. 1
Nominal chemical composition of RR1000 Ni-based superalloy.

Element	Cr	Co	Al	Mo	Ti	Ta	Zr	C	B	Hf	Ni
wt. %	15	18.5	3	5	3.6	2	0.06	0.027	0.015	0.5	Balance
at. %	16.49	17.94	6.35	2.98	4.29	0.63	0.04	0.13	0.08	0.16	Balance

both secondary and tertiary precipitates, but the very low volume fraction of tertiary γ' precipitates means that their contribution will be comparatively small. Two samples aged for different times have been analysed in order to compare precipitate lattice strain at an ageing time corresponding to the maximum mean secondary precipitate size and for the minimum mean secondary precipitate size (as found immediately after splitting). These two samples are referred to as "large-scale precipitates" and "small-scale precipitates", respectively, in Table. 2.

2.3. Microstructure and microanalysis of large γ' precipitates

2.3.1. Defining precipitate classes

Samples were mechanically polished using standard metallographic techniques and finished with a final polish using colloidal silica solution for 30 min in order to obtain the required surface-quality. To reveal the different microstructures using scanning electron microscope (SEM) imaging, specimens were etched using a two-part etchant to dissolve the γ' phase but retain the matrix [28]. High-resolution SEM imaging was performed at 3 kV with a beam current of 0.2 nA using an in-lens detector in the immersion mode fitted into an FEI Magellan 400L field-emission gun (FEG) SEM. Automatic image thresholding was applied within the ImageJ software in order to characterise the precipitate size distributions and quantify these as a function of ageing time [24]. The precipitate size (mean radius) is defined throughout this work as $\sqrt{A/\pi}$ where A represents the measured particle cross sectional area, assuming that particles are nearly spherical. However, these measurements clearly do not reveal the actual precipitate size particularly for precipitates with flower-like morphologies, since the sample surfaces are randomly cut two-dimensional cross-sections through the precipitates' complex three-dimensional structure. Therefore, we have also used a manual size analysis method, applying the same thresholding approach but choosing to analyse only representative precipitates (>20). In order to distinguish the flower-like precipitates from spherical precipitates, the quantity of sphericity, S, was used to characterise the morphology of the precipitates. We define $S = r_{min}/r_{max}$ where r_{min} and r_{max} are respectively the minimum and maximum radii of the precipitate measured from bore to rim. A sphericity value of 1 therefore represents a perfectly spherical particle while a lower value indicates a less symmetric shape. We note that this simple analysis of two dimensional SEM images provides a qualitative means to compare microstructures at different ageing times rather than being an absolute quantification of precipitate morphology.

2.3.2. Measurement of elemental composition in the core of the precipitates

Our previous work has demonstrated semi-quantitative

compositional analysis for γ' precipitates in RR1000 using absorption corrected energy dispersive X-ray (EDX) spectroscopy in the scanning transmission electron microscope (STEM) [24]. Here we employ a similar approach to study size-dependent compositional variations in the as-cooled condition and after ageing. EDX spectroscopy was performed using an Oxford Instruments X-Max^N 80T silicon drift detector (SDD) with a take-off angle of 20° fitted into an FEI Tecnai F30 S/TEM. EDX spectra were acquired from the centre of the extracted precipitates using a convergence semi-angle of 12.5 mrad, a spot size of around 0.8 nm and dwell times of ~3 min in order to obtain >250,000 counts/spectrum. The precipitates typically have diameters of >100 nm giving an interaction volume containing millions of atoms. STEM imaging was performed using an FEI Tecnai F30 S/TEM with an accelerating voltage of 300 kV. High-angle annular dark field (HAADF) imaging was performed with a convergence semi-angle of 12.5 mrad and a HAADF inner angle of 30 mrad.

2.3.3. Local elemental mapping of precipitates and of the γ-γ' interface

Semi-quantitative compositional mapping of free-standing particles using STEM EDX spectroscopy is complicated when the relevant X-ray lines have very different energies (such as Al and Ni) due to the importance of including the appropriate analytical absorption correction factor (ACF) [24,29,30]. For analysis of the local elemental compositional variations present within an individual γ' precipitate we have therefore chosen to compare the ratio of two X-rays having similar but not overlapping energies (Ni-Kα X-rays at 7.47 keV and Co-Kα X-rays at 6.91 keV). The ACF between these two elements will be nearly thickness-independent within an analytical accuracy of 1.5% for a precipitate thickness of 200 nm [24]. To study the elemental distribution at the γ-γ' interface and within the γ matrix surrounding a precipitate, a TEM sample was prepared by focused ion beam (FIB) sectioning. Thickness measurements performed on these cross sectional samples using electron energy loss spectroscopy (EELS) demonstrated values of t/λ of ~1.32–1.38 for both precipitates and matrix suggesting a fairly uniform thickness of ~150–157 nm and therefore allowing EDX absorption correction to be applied using the Cliff-Lorimer thin-film approach [30].

We have employed an FEI Titan G2 80–200 ChemiSTEM™ (S) TEM fitted with an X-FEG high brightness electron source and a Super-X 4 SDD EDX detector system with an elevation angle of ~18°. Spectrum imaging was performed using an accelerating voltage of 200 kV, a convergence semi-angle of 21 mrad and a beam current of 1.2 nA, providing count rates of >50,000 counts/second which enabled pixel-by-pixel semi-quantitative compositional mapping. HAADF imaging in the Titan was performed with a HAADF inner angle of 60 mrad.

Table. 2
Constrained and unconstrained coherency lattice strain measured using synchrotron XRD for microstructures aged to produce small-scale secondary γ' precipitates (immediately after splitting) and large-scale secondary γ' precipitates with maximum mean precipitate size (present immediately prior to splitting). Note that the lattice strain change that is predicted to result from localised compositional variations is also included.

Coherency strain at 1073 K	Small-scale secondary	Large-scale secondary
$a^{\gamma}{}_{bulk}$ (Å)	3.61312	3.61309
$a^{\gamma'}{}_{bulk}$ (Å)	3.61515	3.61520
$a^{\gamma'}{}_{powder}$ (Å)	3.61518	3.61791
$\varepsilon_{constrained}$ (%)	0.057	0.059
$\varepsilon_{unconstrained}$ (%)	0.074	0.133
$\varepsilon_{unconstrained}$-$\varepsilon_{constrained}$ (%)	0.017	0.074
$\varepsilon_{unconstrained}$-$\varepsilon_{constrained}$ (%) predicted from localised compositional variations	/	0.076

3. Results

### 3.1. Microstructural evolution for different ageing times

SEM images revealing the temporal evolution of microstructure within the alloy RR1000 cooled at 100 K/min and aged at 1073 K from 0.5 h to 8.0 h, are shown in Fig. 1. The observed precipitate size distributions (PSDs) are typically bi-modal with small tertiary γ' precipitates (2–25 nm in diameter) and secondary γ' precipitates whose sizes vary as a function of ageing from small-scale secondary with diameters of ~55 $\pm$ 10 nm (found immediately following splitting) to large-scale secondary of 120 $\pm$ 20 nm with a cyclic period of ~2.5 h (Fig. 2). Comparing different measurement methods, automated image analysis tools underestimated the radius of secondary precipitates for flower-shaped large-scale particles by about 25–30% compared to the manual method but produced an acceptable estimation of the radius for small-scale spherical precipitates (Fig. 2a). The sphericity of the precipitates (Fig. 2b) is greatest for the small-scale secondary precipitates (found immediately following splitting) while large-scale precipitates have more flower-like morphologies. Both manual and automatic methods gave similar mean sphericity due to the large experimental scatter in this measurement. The precipitate volume fraction increases from 0.39 to 0.43 within the first splitting cycle (2.5 h) and thereafter remains constant (Fig. 2c). The anomalous cyclic coarsening behaviour of the secondary γ' precipitates is illustrated schematically in Fig. 3 with the precipitates initially growing then splitting into smaller spherical precipitates.

3.2. Lattice changes during ageing

The γ' lattice misfits for the constrained and unconstrained γ' precipitates measured using synchrotron XRD are summarised in Table. 2. The magnitude of the constrained lattice misfit is constant for both large and small secondary γ' precipitates, with a value of ~0.06%. However, the unconstrained γ' lattice parameter of the large-scale γ' precipitates is almost 0.003 Å greater than the unconstrained lattice parameter for small-scale γ' precipitates. Accordingly, the unconstrained misfit for the large-scale γ' is nearly twice that measured for the small-scale precipitates (0.133% compared to 0.074%). The difference in {100} lattice spacing of the small and large-scale γ' powder suggests a significant difference in composition.

3.3. Composition-ageing relationships for γ' precipitates

The compositional variation as a function of precipitate size for the as-cooled microstructure displays similar composition-size relationships to those found previously in this alloy [24,31]. This data refers to the mean composition at the centre of the precipitate. In order to estimate changes in the composition of the secondary precipitates as a function of ageing time a similar analysis has been performed considering the composition of mean sized precipitates as a function of ageing time (Fig. 4). The variation in the elemental composition of the γ' precipitates (Fig 4) is correlated to the cyclic behaviour measured for the precipitate morphology (Figs. 1 and 3). For example, the Al content shows a general increase for longer ageing times but also has local maxima at the 2.5 h time intervals
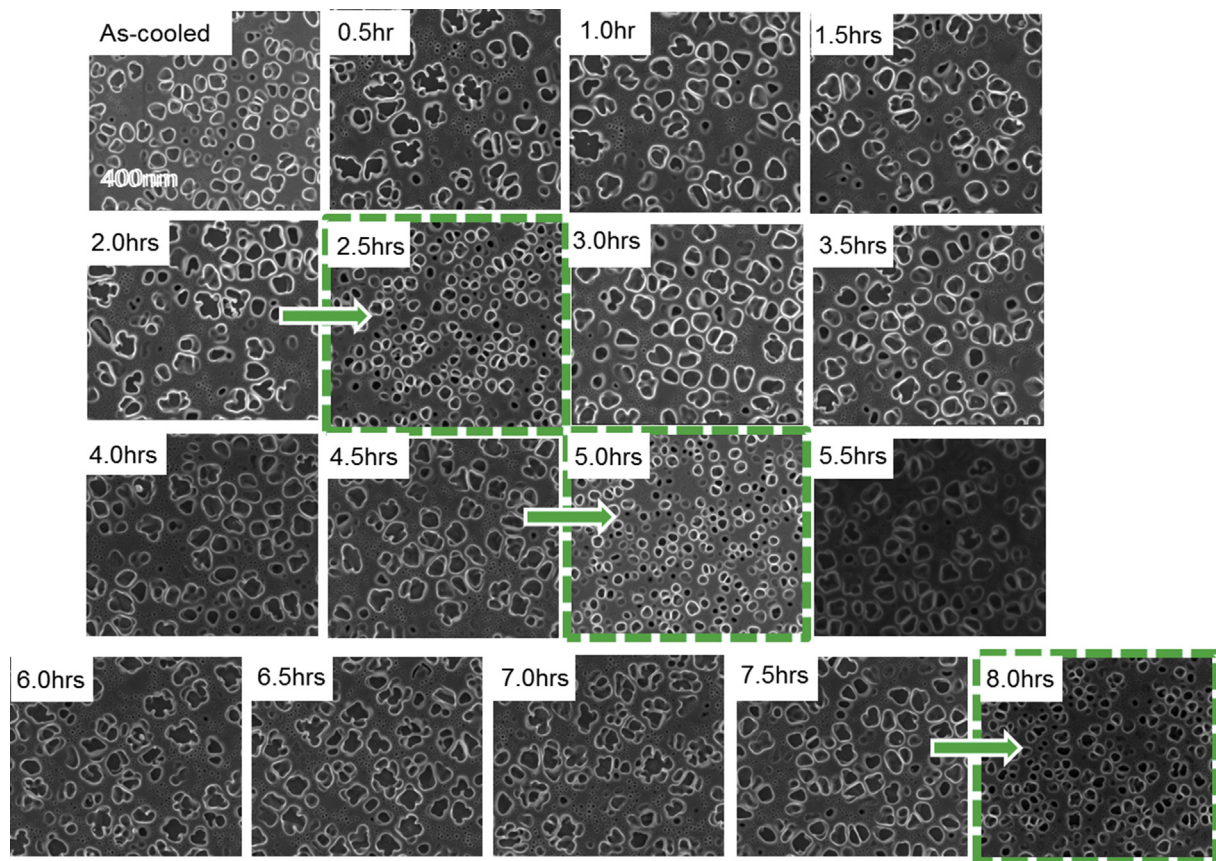
Fig. 1. SEM images illustrating the temporal cyclic evolution of precipitate size distributions (PSDs) produced for the alloy RR1000 after different ageing times from as-cooled to 7.5 h at 1073 K. The green arrows highlight where splitting has occurred at 2.0–2.5 h, at 4.5–5.0 h, and at 7.5–8.0 h annealing times. (For interpretation of the references to colour in this figure legend, the reader is referred to the web version of this article.)
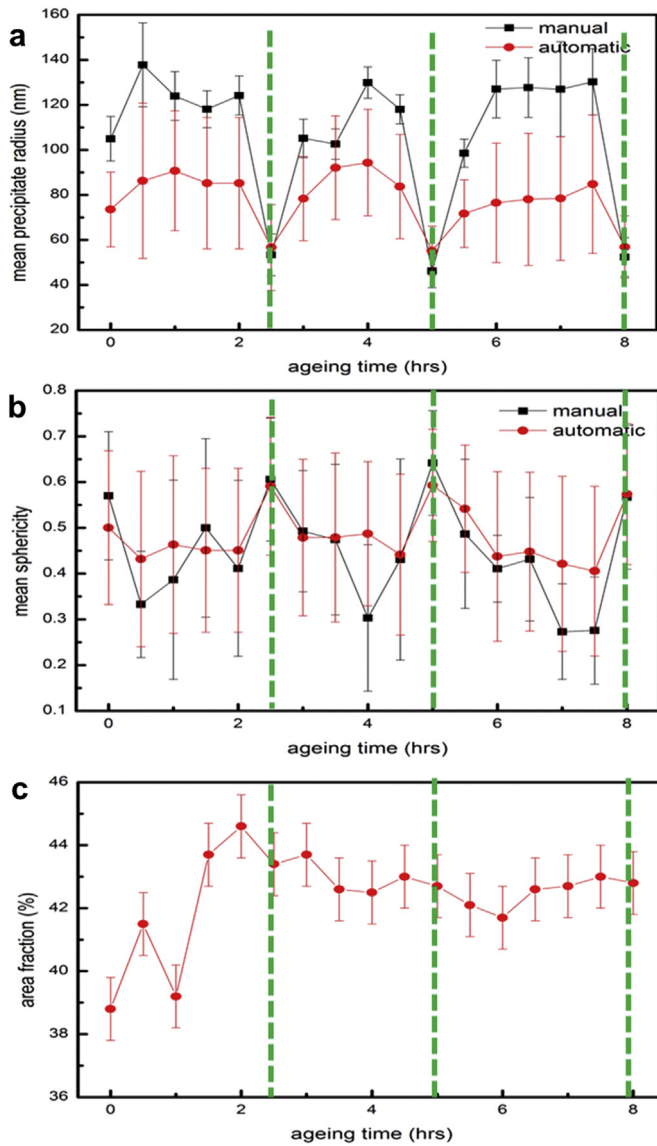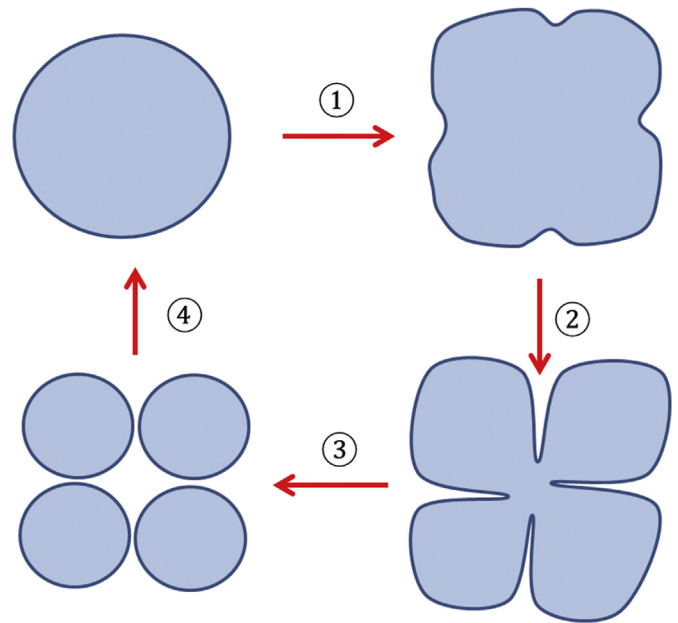
Fig. 2. Analysis of SEM images to determine a) mean radius and b) mean sphericity of secondary γ′ precipitates and c) area fraction of all γ′ precipitates measured as a function of ageing time. Dashed green lines indicate annealing times where splitting has just occurred (Fig. 1). Precipitates with sizes below 40 nm were ignored. Manual and automatic measurement methods are compared. Note that all the precipitate radii are likely to be underestimates due to the image thresholding procedure. (For interpretation of the references to colour in this figure legend, the reader is referred to the web version of this article.)

Fig. 3. Schematic diagram illustrating the how the microstructure of the secondary γ′ precipitates evolves during cyclic coarsening with repeating cycles of precipitate instability (1 + 2), splitting (3) and growth (4).
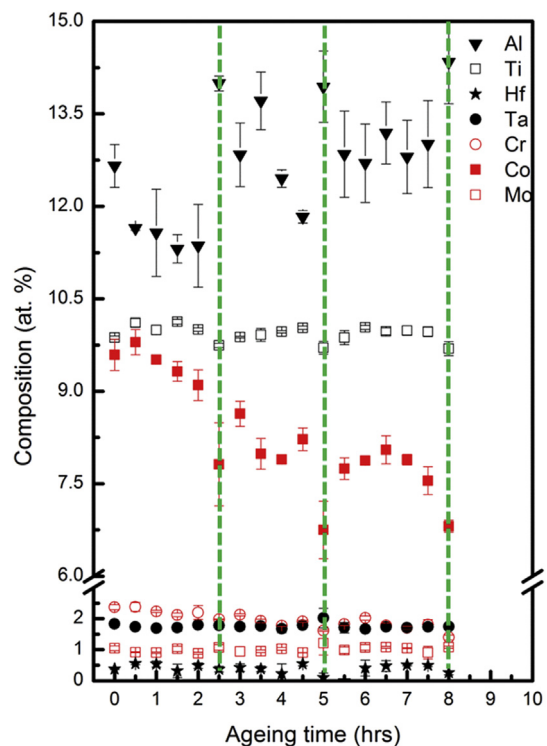
Fig. 4. Compositional variations at the precipitates' centre corresponding to the as-defined typical precipitates' size. The data was extracted from measured size-dependent compositions for each ageing region. The error bars were calculated using the standard deviation of 5–10 particles. Green dashed lines indicate the time intervals where small-scale secondary precipitates are produced by splitting. (For interpretation of the references to colour in this figure legend, the reader is referred to the web version of this article.)

immediately following splitting. In comparison, the Ti content is broadly constant but with local minima at the time intervals immediately following splitting (2.5 h, 5.0 h and 8.0 h). The Co concentration shows the strongest variation during coarsening, decreasing by ~17% from 9.8 at.% Co to 8.1 at.% Co for similarly sized secondary γ′ precipitates at 0.5 h and 6.5 h respectively (Fig. 4). In addition, the Co composition also shows cyclic variations with local minima immediately after precipitate splitting.

3.4. Elemental mapping of individual extracted precipitates

The diffusivities of the major alloying elements in RR1000 differ greatly within the γ′ precipitates compared to those in the γ matrix [24,31]. The exception to this is nickel, which has relatively high diffusivity and similar diffusion coefficients in both γ and γ′. Nickel

is therefore expected to maintain a homogeneous elemental distribution in γ′ so it provides an effective normalisation element for comparing Co concentration within the γ′ precipitates. Fig. 5 uses
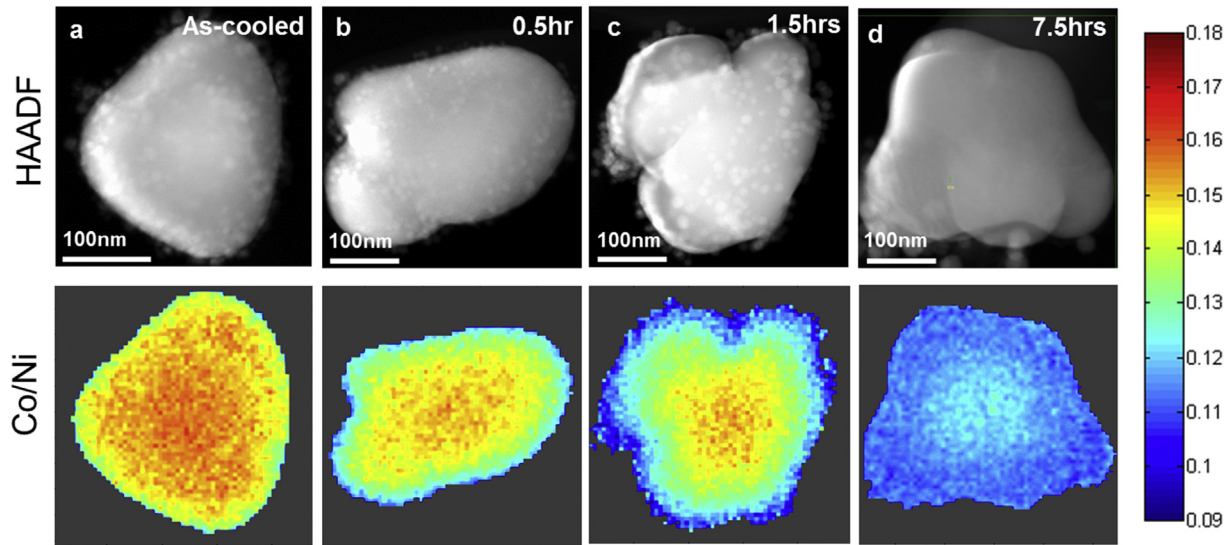
Fig. 5. HAADF images (top), and X-ray count ratio map of Co/Ni (bottom) according to the temperature scale (right side of the maps). Comparing the ratio maps of large-scale secondary precipitate at different ageing time a) as-cooled, b) 0.5 h, c) 1.5 h and d) 7.5 h shows the reduced chemical inhomogeneities. It is noted that the limited number of small particles agglomerated onto these particles do not contribute significantly to ratio maps.

the ratio of Co/Ni net X-ray counts (Co-Kα with 6.91 keV, Ni-Kα with 7.47 keV) measured as a function of position within the STEM-EDX spectrum image to reveal the Co distribution within an individual extracted precipitate. The Co distribution for a typical as-cooled γ′ precipitate is shown in Fig. 5a, while that for three similarly sized γ′ precipitates present at different ageing times (0.5 h, 1.5 h and 7.5 h) are compared in Fig. 5b, c and d respectively. Interestingly, all the precipitates have a greater Co concentration in the centre compared to the outer regions. In addition, the peak Co/Ni ratio was 1.7 in the core of the particle aged for 0.5 h but just 1.3 for the particle aged for 7.5 h, suggesting that the Co concentration is becoming more uniform towards equilibrium with ageing.

Fig. 6 shows the differences in Co distribution for different morphologies of γ′ precipitate extracted from the microstructure aged for 7.5 h. Both the large secondary γ′ precipitates have a greater Co concentration in the centre of the precipitate compared to the outer regions (Fig. 6a,b) while the small secondary precipitate (Fig. 6c) has a lower and more uniform composition.

3.5. Elemental mapping of the γ-γ′ interface and surrounding region

We have used a FIB cross sectional sample to investigate compositional segregation at the γ-γ′ interface using STEM-EDX spectrum imaging (Fig. 7a–f). The elemental maps processed from the full spectrum image show that close to the γ′ precipitate the matrix is locally enriched in Cr (Fig. 7b) and Co (Fig. 7c) but depleted in Al (Fig. 7e) and Ti (Fig. 7f). An elemental line scan extracted from the spectrum image normal to the γ-γ′ interface (Fig. 7g) shows that the enrichment extends ~45 nm into the matrix with the peak enrichment corresponding to a 4.5 at. % increase in Co and Cr, and a decrease in Al and Ti content of 2.2 at. % and 1.2 at. % respectively, compared to the far field matrix composition. Importantly, this variation in local elemental composition is larger than anything that has been previously reported [8,12,32–34].

4. Discussion

We have demonstrated that RR1000 cooled at 100 K/min from a γ′ supersolvus heat treatment undergoes three rounds of cyclic
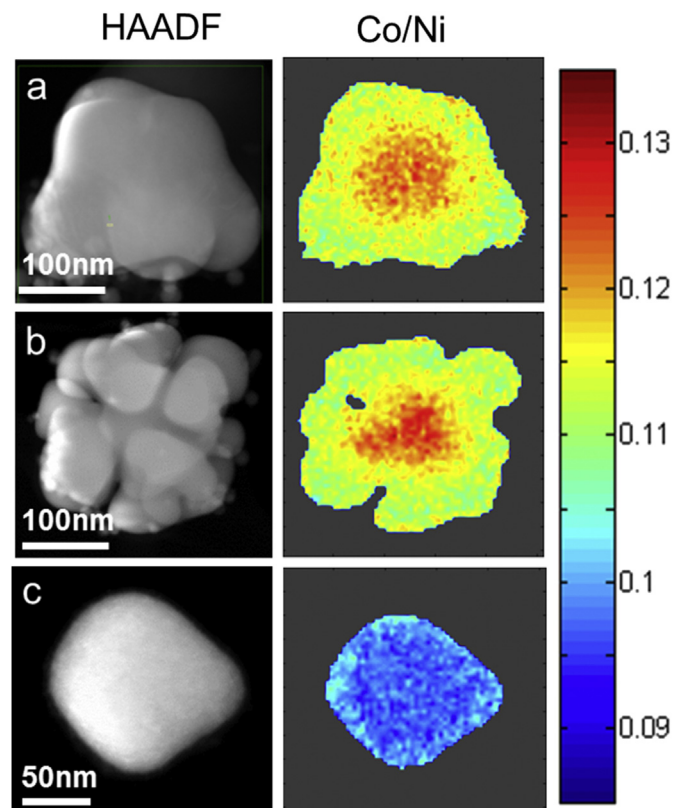
Fig. 6. HAADF images (left), and X-ray count ratio maps of Co/Ni (right) plotted using the temperature scale shown far right comparing the Co elemental distribution in different precipitate morphologies observed in the microstructure after 7.5 h ageing. a) Prior to splitting b) for a strongly flower-like morphology (deeply-split) and c) for a small sphere assumed to be formed after splitting.

coarsening and reversal coarsening when aged for 8 h at 800 °C, with distinct splitting (reversal coarsening) of the large-scale secondary γ′ precipitates (between 0.5 and 2.5 h, 3.5–5.5 h and 6.0–8.0 h), and coarsening (between 2.5–3.0 h and 5.0–5.5 h), respectively. In fact, this cyclic reversal coarsening behaviour was
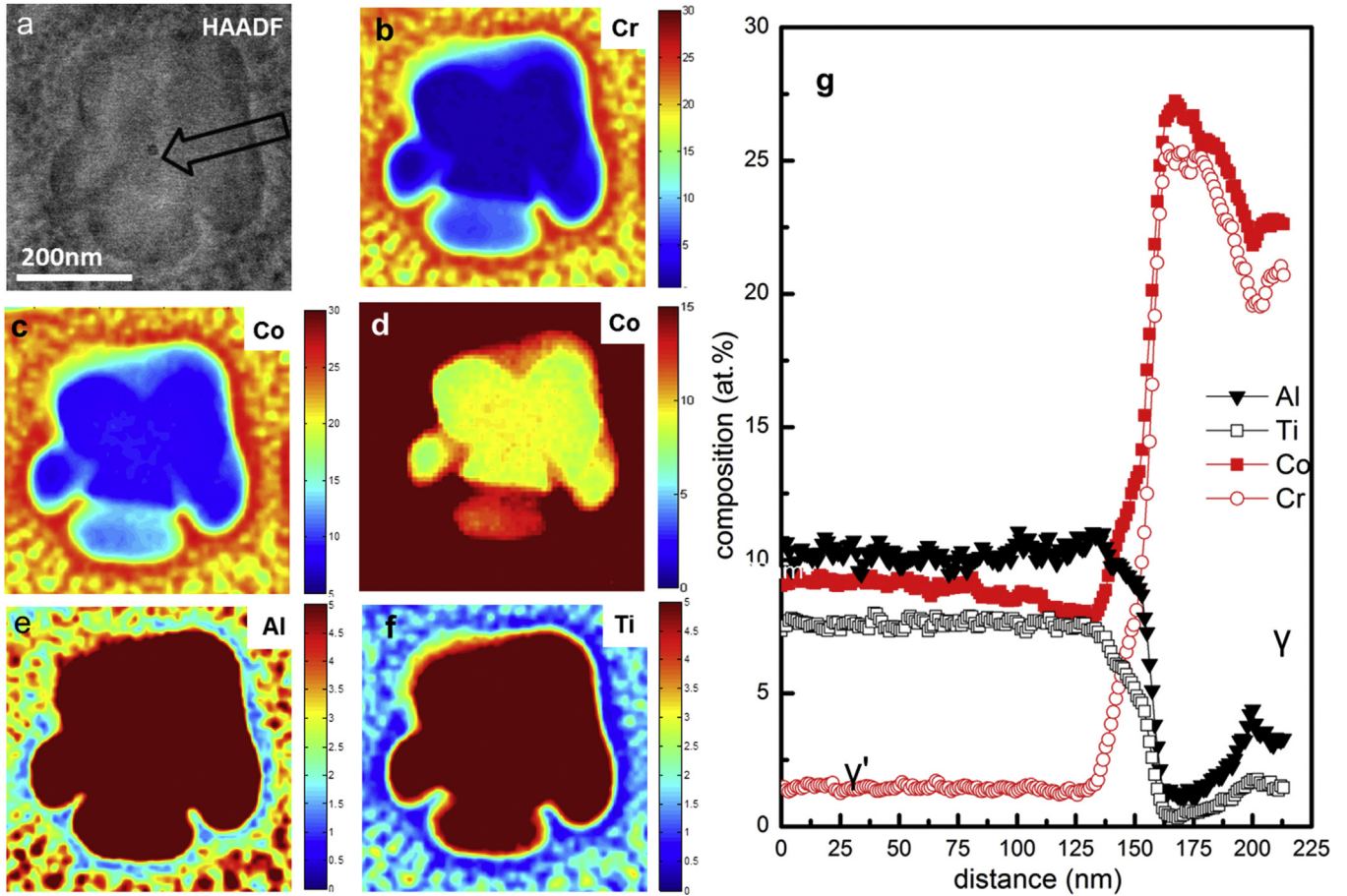
Fig. 7. HAADF image a) of a FIB-sectioned thin foil and corresponding quantified EDX elemental maps of b) Cr, c) Co, d) replot of Co using a different colourmap to reveal the details within γ′, e) Al and f) Ti. g) is the extracted elemental line profile across an interface labelled by the black hollow arrow in (a). Note that there is no well-defined γ-γ′ interface visible from the compositional variation.

demonstrated to continue beyond 8 h and cyclic behaviour was found to still be present after 24 h ageing at this temperature [20]. In RR1000, the γ′ precipitates can be assumed to have a composition of $(Ni,Cr,Co,Mo)_3(Al,Ti,Ta,Hf)$ [24,31].

The equilibrium Co solubility of γ′ decreases with decreasing temperature [31]. The core of a large-scale secondary precipitate is expected to have formed at relatively high temperature and is therefore expected to have a higher Co equilibrium composition than the outer parts of the precipitates which formed later and at lower temperature. This explains the enrichment of Co in the core of the larger γ′ precipitates that is demonstrated in Fig. 5a. The large decrease in the Co content measured for the core of the γ′ precipitates (Fig. 4a) suggests that Co was initially supersaturated, and moves towards a lower equilibrium concentration during ageing. The lowest Co content (6.8 at. %) is found in the small-scale secondary γ′ and is the same at 5.0 h and at 8.0 h suggesting that this is close to the equilibrium value. Our thermodynamic calculations using ThermoCalc predict a higher equilibrium Co composition of 8.2 at. % for the γ′ precipitates at 1073 K [35]. However, we note that thermodynamic calculations for absolute equilibrium concentration can often be inaccurate for multi-component alloy systems [31,36]. More reliable are thermodynamic predictions of chemical potentials based on experimentally measured elemental compositions.

We calculate that the experimentally observed decrease in Co concentration (from 9.8 at.% Co to 6.8 at. %) is predicted to change the chemical potential by ~2.4 × 10^3 J/mol (where Co is assumed to substitute on the Ni sublattice). In comparison, the +4.5 at. % Co

enrichment that we observed in the γ matrix close to the γ-γ′ interface (Fig. 7), is predicted to change the chemical potential by a smaller amount (~0.84 × 10^3 J/mol) illustrating that the chemical driving force favours the diffusion of Co out of the precipitates and into the matrix.

We must now consider how diffusion will contribute to the observed elemental segregation at the γ-γ′ interface. In multi-component systems, the elemental interdiffusivity is given by $D_{jk} = \sum_i M_{ki} \frac{\partial^2 \mu}{\partial C_i \partial C_j}$ [17], where D_{jk}, M_{jk}, μ and C_j are the interdiffusivity, the mobility, the chemical free energy and elemental concentration, respectively. The estimated interdiffusivities for Co in Ni within γ′ and γ are ~1.6 × 10^{-19} m²/s and ~3.7 × 10^{-19} m²/s using data from the mobility database [17] and our calculated change in chemical potential. This allows estimation of the diffusion distances, $d = \sqrt{(2Dt)}$ for a given time, t, as shown in Table. 3. This data shows that in the γ′ precipitates Co can only diffuse 54 nm within one

Table. 3
Estimated diffusion distance of Co in γ and γ′ as a function of ageing time at 1073 K.

Time (hrs)	γ (nm)	γ′ (nm)
0.5	36	24
1.0	51	34
1.5	63	42
2.0	72	48
2.5	81	54

complete cycle (2.5 h), while the radius of the large-scale secondary γ' is ~120 nm. This relatively low diffusivity prevents the homogenisation of the large-scale secondary γ' within one period: instead the Co inhomogeneity gradually decreases upon ageing as shown in Fig. 5a–d.

The estimated diffusion distance for Co in the γ matrix is ~81 nm within one period, which compared favourably with the width of the interfacial enrichment. Importantly, Campbell et al. have demonstrated that in Ni based superalloys Co has a negative chemical interdiffusivity in the presence of other alloying elements (Cr, Al, Ti) [17]. Therefore Co enrichment at the interface will slow down the interdiffusion of Cr, Al, and Ti compared to matrix regions far from the interface and could therefore lead to the observed depletion in Al and Ti close to the interface (Fig. 7), The depletion of γ' stabilisers (Al and Ti) near the γ/γ' interface will have the further effect of slowing down the growth of γ' and could therefore explain the absence of significant growth in the size of secondary precipitates for the ageing described here (Fig. 2a). Campbell et al.'s interdiffusion matrix also predicts that reduced Al and Ti will slow down the diffusion of Co [17] such that is takes longer to homogenise Co enrichment at the interface.

The rapid changes in Co from small-scale secondary to large-scale secondary, occurring within just 0.5 h (Fig. 4), is likely to result from the rapid γ' growth into a Co rich γ matrix, correlated with a >50 nm increase in precipitate size immediately following splitting. Table. 3 predicts a diffusion distance for Co of 36 nm and 24 nm in 0.5 h within γ and in γ' respectively. Comparing these two values supports our experimental observations that the growing large-scale secondary γ' continue to be supersaturated in Co even after a complete coarsening cycle. The drive towards a more homogenised composition as ageing continues will favour longer cycling times and indeed this is observed experimentally in Figs. 1 and 2 (the first and second cycles are 2.5 h but the third one is 3.0 h). However, none of this discussion explains the anomalous precipitate splitting behaviour.

Vogel et al. [37] have proposed that the splitting of γ' can be caused by formation of γ inside the γ' precipitates. However, we find no evidence to suggest that this is occurring in our material. Our compositional measurements obtained from the precipitates' cores (Fig. 4) showed high concentrations of γ' stabilisers (Al ~12–14 at.%, Ti ~10 at.%, Ta ~1–2 at.%). The sums of these γ' stabiliser elements are close to the expected stoichiometry of γ', therefore indicating there is no γ formation within these γ' precipitates. In addition, analysis of our STEM, TEM and SEM images as well as quantitative investigation of corresponding TEM electron diffraction data did not reveal any evidence of γ formation inside the γ' precipitates, suggesting that this is not the splitting mechanism in the present case. Energetically, splitting is favourable when the decrease in elastic strain energy of the system more than compensates for the increase in interfacial energy produced [22]. Elastic and interfacial energy considerations have been used to explain γ' splitting (reversal coarsening) for cuboidal γ' in Ni-based superalloys [3,21]. However, the explanation is less clear for alloys like RR1000 where the composition is tuned to produce a negligible γ-γ' misfit minimising lattice strain such that the γ' precipitates tend to be spherical.

In Ni-based superalloys the effect of elastic modulus is negligibly small because both γ and γ' have nearly identical elastic constants [38]. Ignoring the contribution of chemical free energy, the driving force for coarsening in a system containing a large volume fraction of precipitates is [23]:

$$\Delta G = \Delta E_{interfacial} + \Delta E_{self} + \Delta E_{interaction}$$

Where ΔG is the total free energy, ΔE_{self} is the elastic self-energy

resulting from coherency strain but ignoring any contribution from precipitate–precipitate interactions, $\Delta E_{interfacial}$ is the interfacial energy given as $2\tau/r$ (τ is the interfacial tension and r is the precipitate radius) and $\Delta E_{interaction}$ is the elastic interaction energy resulting from neighbouring precipitates in high volume fraction systems. Khachaturyan et al. have described a method for predicting the total elastic interaction energy ($\Delta E_{self} + \Delta E_{interaction}$) based on micro-elasticity theory as [23]:

$$\Delta E_{total} = \alpha V E_1$$
$$= \alpha V \left(-\frac{1}{2}(C_{11} + 2C_{12})^2 C_{11} - C_{12} \right.$$
$$\left. - 2C_{44} \frac{\in_{unconstrained}^2}{C_{11}(2C_{11} + C_{12} + 2C_{44})} \right)$$

Where V is the precipitate volume, α is a factor related to precipitate shape (which has a value of 0.709 for a sphere but 0.436 in a cube) and E_1 is the elastic energy density. C_{11}, C_{12} and C_{44} are the cubic elastic constants of the γ' phase [23]. This predicts that the total elastic energy is proportional to the square of the unconstrained lattice strain between precipitates and matrix phase. Our synchrotron XRD measurements have shown that the constrained coherency strain for the differently sized precipitates is similar (0.057% for the large-scale precipitates compared to 0.059% for the small-scale) but the unconstrained lattice strain is much larger for the large-scale precipitates (0.133% compared to 0.074% for the smaller precipitates) (Table. 2). This demonstrates that in this alloy the elastic lattice strain increases as the precipitate size increases, overwhelming the reduced interfacial energy for a particular size of precipitate, which results in the observed morphological instability. The critical radius for large-scale secondary precipitate splitting as a function of assumed unconstrained lattice strain has been calculated as shown in Fig. 8, using elastic constants from Ref. [23] and considering a simple model where a large spherical precipitate splits into 8 smaller spherical precipitates each with half the radius of the large sphere. Using the measured unconstrained strain and comparing this with the sum of interfacial energy and elastic strain energy would suggest a critical radius of ~200 nm for γ' splitting, which is similar to the largest precipitates seen in our samples. For example, the precipitates mapped in Figs. 6 and 7 have an average
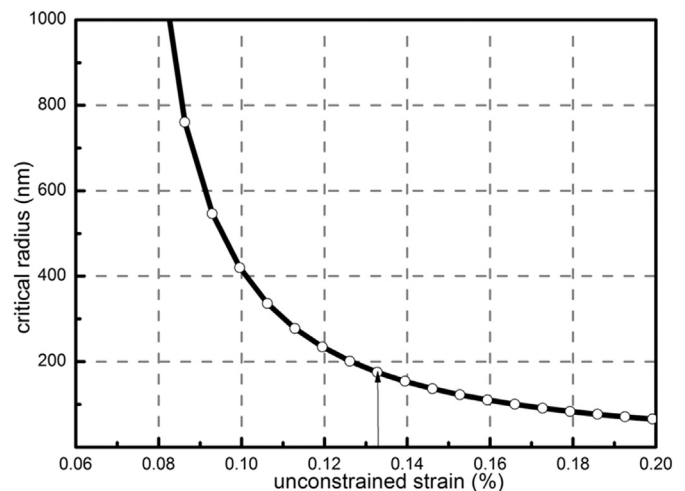

Fig. 8. Calculated critical splitting size of precipitates as a function of unconstrained strain. Grey arrow points to the corresponding critical size with respect to experimentally measured unconstrained lattice strain.

radius of ~140−180 nm. In fact, Doi et al. have demonstrated that the elastic strain energy could drive the splitting to occur along the most elastically compliant <001> directions when a large-scale cuboidal precipitate transits to an octet [3,21]. We have found the same splitting direction (<001>) in this particular case of near spherical precipitates, as demonstrated from the our electron diffraction analysis of an individual large-scale secondary precipitate (Fig. 9), which further supports our conclusion that elastic strain energy causes this splitting (reversal coarsening). However, the unexpected observation of significant elastic strain in RR1000, which at equilibrium is a 'near-zero' misfit alloy requires further consideration.

Synchrotron X-ray diffraction analysis in Table. 2 only provides average constrained or unconstrained lattice spacings for the two phases assuming homogeneous composition. Our elemental mapping demonstrates that in fact this assumption is not valid, particularly near the γ/γ' interface. Ti compositional variations will have the largest effect on the γ' lattice parameter, while the combination of Al and Ti content will have the greatest effect on the lattice parameter of the γ matrix [39]. The contribution of other elemental additions to the lattice parameter may be neglected either because they are present in very low concentrations or because they do not significantly alter the lattice parameter of either γ or γ' [39]. Immediately after splitting the precipitates have a composition that is decreased by 0.35 at.% Ti and 1.9 at% Co, and increased by 1 at.% Al (Fig. 5). Using data from Ref. [39] it can be predicted that this compositional variation will yield an increase in lattice mismatch of 0.02 Å and hence an increased strain of 0.06%, which is in good agreement with the experimentally measured difference between the constrained and unconstrained strain for the large-scale secondary precipitates (0.074% as shown in Table. 2).

The elemental segregation in the γ matrix close to the γ-γ' interface (+4.5 at. % Co, +4.5 at. % Cr, −2.2 at. % Al and −1.2 at. % Ti as shown in Fig. 7), will produce a local decrease of 0.0028 Å in the γ lattice and hence cause a reduction of γ lattice in this region by 0.077%, as estimated according to Vegard's law and using the coefficients in Ref. [39]. As shown schematically in Fig. 10, this will further increase the γ/γ' lattice mismatch at the interface, which cannot be detected by the bulk X-ray diffraction analysis. Consequently, the local mismatch between γ and large-scale secondary γ' will be larger than one would calculate from simply considering the mean alloy composition and hence the γ' splitting mechanism (reversal coarsening) is likely to be the result of compressive stresses in γ'.

5. Conclusion

In conclusion we can summarise the observed anomalous cyclic behaviour that is illustrated schematically in Fig. 3 as follows:

1) In the as-cooled microstructure secondary γ' precipitates are supersaturated in Co. As coarsening growth occurs, Co diffuses into the matrix but the limited diffusivity of Co in γ' and γ results in an inhomogeneous non-equilibrium elemental distribution.
2) The precipitates show elemental enrichment of Co in the core while the matrix shows enrichment of Co at the γ'/γ interface. This interface enrichment further impedes the diffusion of other elements, creating Cr enrichment and Al and Ti depletion at the interface, which in turn causes a local change in lattice parameter at the interface.
3) The resulting large lattice misfit generates high elastic strain, causing the precipitates to split along the most elastically
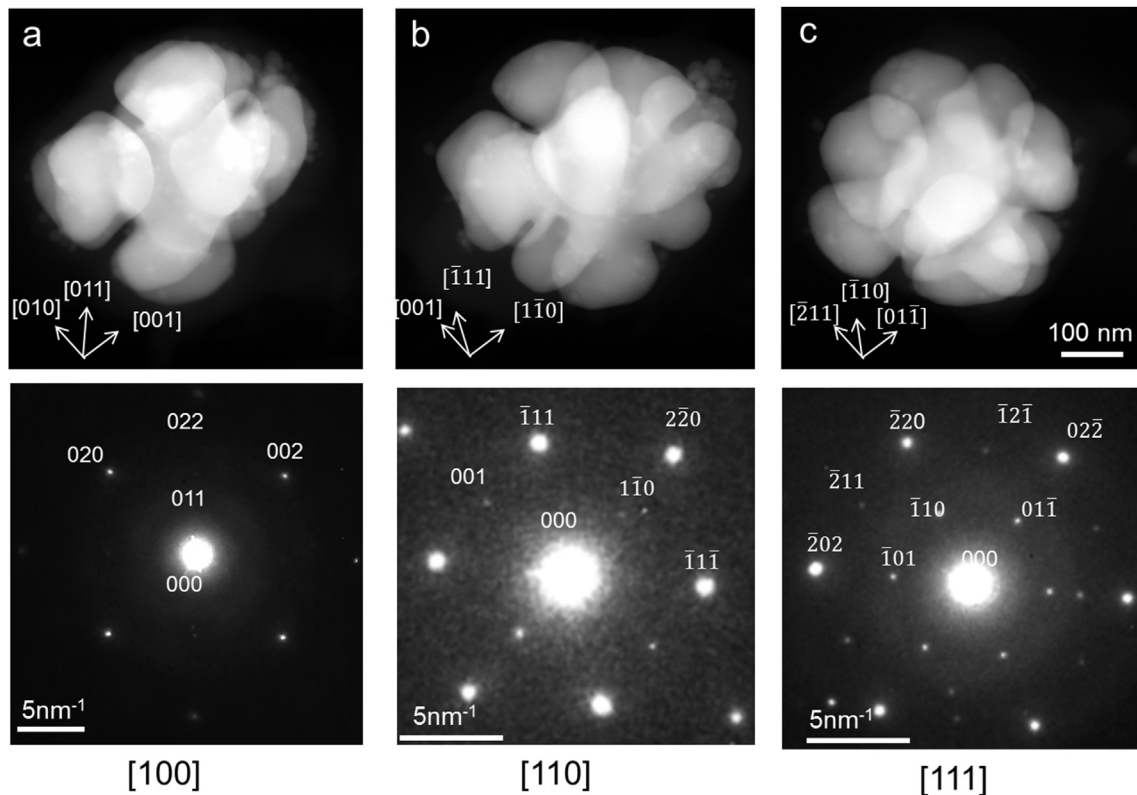
Fig. 9. Top row: large-scale secondary precipitate with the typical flower-like morphology observed immediately prior to splitting viewed along a) <100>, b) <110> and c) <111> directions. Below the images are shown the corresponding electron diffraction patterns. This indicates the orientation of splitting is <100> consistent with typical octet-type splitting and suggesting that there may be 8 smaller spherical precipitates formed after splitting.
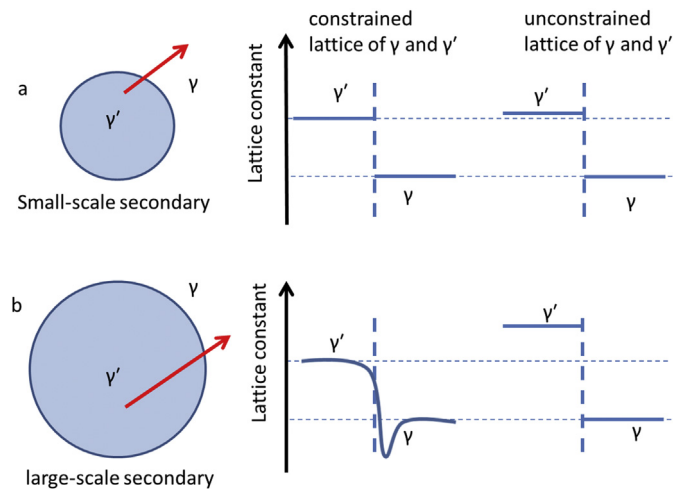
Fig. 10. Schematic diagram illustrating the relative magnitudes of the constrained and unconstrained elastic constraints for different sized precipitates: a) small-scale secondary γ' and b) large-scale γ'. Line scans illustrate the variation of lattice constant in the constrained case (centre) and unconstrained case (right) as a function of distance from the precipitate centre (red arrow). Dashed lines indicate the averaged constrained lattice constants of γ and γ'. (For interpretation of the references to colour in this figure legend, the reader is referred to the web version of this article.)

compliant directions such that a morphological transition is observed after ~2.5 h heat treatment.

4) After splitting the small-scale precipitates initially grow, so as to drive precipitate towards equilibrium compositions and also to reduce the total interfacial energy, consistent with normal coarsening behaviour. However, the limited diffusivities mean that there is insufficient time during a single cycle for the precipitate composition to completely homogenise and so elemental segregation persists, leading to higher elastic energy and precipitate's morphology instability so that the cycle repeats. This observed cyclic behaviour is expected to continue until the composition is homogenised.

In this work, we have used absorption-corrected STEM EDX spectroscopy and ex-situ synchrotron XRD to study the abnormal cyclic coarsening behaviour observed when ageing the PM Ni-based superalloy RR1000 at 1073 K following a cooling rate of 100 K/min. The cyclic behaviour occurs because the limited diffusion kinetics in γ and γ' induces compositional supersaturation within large-scale secondary γ', and because elemental segregations build up in the γ matrix at the γ-γ' interface creating a large mismatch that is unexpected when considering only the mean alloy composition. Limited elemental diffusivities prevent a homogenous elemental distribution being achieved within a ~2.5 h single cycle and thus the cyclic behaviour continues over many hours.

These findings demonstrate the importance of considering the full complex alloy chemistry and elemental diffusion kinetics, as well as thermodynamics (elastic energy and interfacial energy) when considering microstructural evolution in commercial Ni superalloys.

References

[1] T. Murakumo, T. Kobayashi, Y. Koizumi, H. Harada, Creep behaviour of Ni-base single-crystal superalloys with various γ' volume fraction, Acta Mater. 52 (2004) 3737–3744.
[2] R.C. Reed, The SuperAlloys Fundamentals and Applications, Cambridge University Press, 2006.
[3] M. Doi, Coarsening Behaviour of Coherent Precipitates in Elastically Constrained Systems —With Particular Emphasis on Gamma-Prime Precipitates in Nickel-Base Alloys, Mater. T JIM 33 (1992) 637–649.
[4] M.V. Acharya, G.E. Fuchs, The effect of long-term thermal exposures on the microstructure and properties of CMSX-10 single crystal Ni-base superalloys, Mater. Sci. Eng. A 381 (2004) 143–153.
[5] A.J. Ardell, Precipitation hardening, MTA 16 (1985) 2131–2165.
[6] A. Baldan, Review progress in Ostwald ripening theories and their applications to nickel-base superalloys Part I: Ostwald ripening theories, J. Mater. Sci. 37 (2002) 2171–2202.
[7] A. Baldan, Review Progress in Ostwald ripening theories and their applications to the γ'-precipitates in nickel-base superalloys Part II Nickel-base superalloys, J. Mater. Sci. 37 (2002) 2379–2405.
[8] A.R.P. Singh, S. Nag, J.Y. Hwang, G.B. Viswanathan, J. Tiley, R. Srinivasan, H.L. Fraser, R. Banerjee, Influence of cooling rate on the development of multiple generations of γ' precipitates in a commercial nickel base superalloy, Mater. Charact. 62 (2011) 878–886.
[9] S.N.J.Y. Hwang, A.R.P. Singh, R. Srinivasan, J. Tiley, H.L. Fraser, R. Banerjee, Evolution of the γ/γ' interface width in a commercial nickel base superalloy studied by three-dimensional atom probe tomography, Scr. Mater. 61 (2009) 92–95.
[10] R. Srinivasan, R. Banerjee, J. Hwang, G. Viswanathan, J. Tiley, D. Dimiduk, H. Fraser, Atomic Scale Structure, Chemical Composition, across Order-Disorder Interfaces, Phys. Rev. Lett. 102 (2009).
[11] A.J. Ardell, Quantitative predictions of the trans-interface diffusion-controlled theory of particle coarsening, Acta Mater. 58 (2010) 4325–4331.
[12] A.J. Ardell, V. Ozolins, Trans-interface diffusion-controlled coarsening, Nat. Mater 4 (2005) 309–316.
[13] B.S. Bokstein, S.Z. Bokstein, I.T. Spitsberg, Ni self-diffusion in alloyed Ni_3Al, Intermetallics 4 (1996) 517–523.
[14] J. Cermak, A. Gazda, V. Rothova, Interdiffusion in ternary Ni_3Al/Ni_3Al-X diffusion couples with X=Cr, Fe, Nb and Ti, Intermetallics 11 (2003) 939–946.
[15] J. Cermak, V. Rothova, Concentration dependence of ternary interdiffusion coefficients in Ni_3Al/Ni_3Al–X couples with X=Cr, Fe, Nb and Ti, Acta Mater. 51 (2003) 4411–4421.
[16] M. Karunaratne, P. Carter, R. Reed, On the diffusion of aluminium and titanium in the Ni–Al–Ti system between 900 and 1200° C, Acta Mater. 49 (2001) 861–875.
[17] C. Campbell, W. Boettinger, U. Kattner, Development of a diffusion mobility database for Ni-base superalloys, Acta Mater. 50 (2002) 775–792.
[18] A.J. Ardell, Gradient energy, interfacial energy and interface width, Scr. Mater. 66 (2012) 423–426.
[19] D.A. Porter, K.E. Easterling, Phase Transformations in Metals and Alloys, CRC press, 1992.
[20] R. Mitchell, M. Preuss, S. Tin, M. Hardy, The influence of cooling rate from temperatures above the γ' solvus on morphology, mismatch and hardness in advanced polycrystalline nickel-base superalloys, Mater. Sci. Eng. A 473 (2008) 158–165.
[21] M. Doi, T. Miyazaki, T. Wakatsuki, The effect of elastic interaction energy on the morphology of γ' precipitates in nickel-based alloys, Mater. Sci. Eng. 67 (1984) 247–253.
[22] D. Banerjee, R. Banerjee, Y. Wang, Formation of split patterns of gamma prime precipitates in Ni-Al via particle aggregation, Scr. Mater. 41 (1999).
[23] A. Khachaturyan, S. Semenovskaya, J. Morris Jr., Theoretical analysis of strain-induced shape changes in cubic precipitates during coarsening, Acta Metall. 36 (1988) 1563–1572.
[24] Y.Q. Chen, T.J.A. Slater, E.A. Lewis, E.M. Francis, M.G. Burke, M. Preuss, S.J. Haigh, Measurement of size-dependent composition variations for gamma prime (γ') precipitates in an advanced nickel-based superalloy, Ultra-microscopy 144 (2014) 1–8.
[25] A.N. Fitch, The high resolution powder diffraction beam line at ESRF, J. Res. Natl. Inst. Stan 109 (2004) 133–142.
[26] M. Daymond, M. Preuss, B. Clausen, Evidence of variation in slip mode in a polycrystalline nickel-base superalloy with change in temperature from neutron diffraction strain measurements, Acta Mater. 55 (2007) 3089–3102.
[27] J. Tiley, R. Srinivasan, R. Banerjee, G. Viswanathan, B. Toby, H. Fraser, Application of X-ray and neutron diffraction to determine lattice parameters and precipitate volume fractions in low misfit nickel base superalloys, Mater. Sci. Tech. 25 (2009) 1369–1374.
[28] M. Preuss, P.J. Withers, J.W.L. Pang, G.J. Baxter, Inertia welding nickel-based superalloy: Part I. Metallurgical characterization, Metall Mat Trans A 33 (2002) 3215–3225.
[29] M. Watanabe, Z. Horita, M. Nemoto, Absorption correction and thickness

determination using the ζ factor in quantitative X-ray microanalysis, Ultra-microscopy 65 (1996) 187–198.

[30] M. Watanabe, D. Williams, The quantitative analysis of thin specimens: a review of progress from the Cliff-Lorimer to the new ζ-factor methods, J. Microsc-Oxford 221 (2006) 89–109.

[31] Y.Q. Chen, E. Francis, J. Robson, M. Preuss, S.J. Haigh, Compositional variations for small-scale gamma prime (γ′) precipitates formed at different cooling rates in an advanced Ni-based superalloy, Acta Mater. 85 (2015) 199–206.

[32] J.Y. Hwang, S. Nag, A.R.P. Singh, R. Srinivasan, J. Tiley, H.L. Fraser, R. Banerjee, Evolution of the γ/γ′ interface width in a commercial nickel base superalloy studied by three-dimensional atom probe tomography, Scr. Mater. 61 (2009) 92–95.

[33] C. Booth-Morrison, Y. Zhou, R.D. Noebe, D.N. Seidman, On the nanometer scale phase separation of a low-supersaturation Ni–Al–Cr alloy, Philos. Mag. 90 (2010) 219–235.

[34] C.K. Sudbrack, K.E. Yoon, R.D. Noebe, D.N. Seidman, Temporal evolution of the nanostructure and phase compositions in a model Ni-Al-Cr alloy, Acta Mater. 54 (2006) 3199–3210.

[35] J.-O. Andersson, T. Helander, L. Höglund, P. Shi, B. Sundman, Thermo-Calc & DICTRA, computational tools for materials science, Calphad 26 (2002) 273–312.

[36] N. Dupin, B. Sundman, A thermodynamic database for Ni-base superalloys, Scand. J. Metall. 30 (2001) 184–192.

[37] F. Vogel, N. Wanderka, Z. Balogh, M. Ibrahim, P. Stender, G. Schmitz, J. Banhart, Mapping the evolution of hierarchical microstructures in a Ni-based super-alloy, Nat. Commun. 4 (2013).

[38] Y. Wang, D. Banerjee, C. Su, A. Khachaturyan, Field kinetic model and com-puter simulation of precipitation of L1< sub> 2 ordered intermetallics from fcc solid solution, Acta Mater. 46 (1998) 2983–3001.

[39] P. Caron, High y'solvus new generation nickel-based superalloys for single crystal turbine blade applications, Superalloys (2000) 737–746.